MONITORING AND QUANTIFYING HEAT LOSS FROM SIGNIFICANT GEOTHERMAL AREAS VIA REMOTE SENSING

Chris Bromley[1], Salman Ashraf[2], Anya Seward[1], Rob Reeves[1]

[1]GNS Science, Wairakei Research Centre, Private Bag 2000, Taupo, New Zealand

[2]GNS Science, Box 30-368, Lower Hutt, New Zealand

c.bromley@gns.cri.nz

Keywords: *monitoring, heat-loss, satellite remote-sensing, thermal infra-red, calorimeter, Karapiti.*

ABSTRACT

Accurate assessment of natural heat loss from significant geothermal areas is essential for providing data to improve reservoir simulation and model calibration. Uncertainty in this parameter can lead to large uncertainty in resource assessments and in predictions of sustainable utilisation rates. Monitoring of surface heat-loss changes during production is equally important for history-matching of reservoir models and for assessment of environmental effects. New methods are under development for making better use of thermal infrared imagery from the newly launched Landsat-8 satellite, which has improved in quality and frequency (in tandem with Landsat-7). Along with ground-truth measurements, and high-resolution air-borne infrared surveys, these data are expected to achieve a long-term improvement in the determination of natural and induced changes in surface heat loss.

Issues currently being addressed to assist with better heat flux estimates using remote sensing techniques include: accounting for surface emissivity variations and ambient (background) solar radiation; calibration against surface temperatures of water-bodies; and using optimized algorithms for atmospheric correction (split or mono window). With respect to heat-loss assessment, issues include: accounting for convective vapour loss; and dealing with spatial resolution issues. Integration of imagery with spot measurements of total heat-flux from areas of weakly steaming ground is challenging. This paper summarizes efforts to date in resolving these issues, and provides some examples of heat-loss assessments from Karapiti thermal area (Craters of the Moon), Wairakei, New Zealand.

1. INTRODUCTION

Areas of steaming ground originate from discharges of geothermal vapour through the surface. The steam heats the groundwater, interacts with rainfall, and can transfer large amounts of thermal energy, amounting, in places, to several hundred megawatts. Accurately quantifying and monitoring such heat-loss is very difficult, and can be time-consuming and expensive. However, heat-loss data is becoming ever more important for calibrating (that is, history matching) reservoir simulation models, for the purposes of better predicting the long-term effects on significant surface geothermal features of future development scenarios (Newson & O'Sullivan, 2004, Newson, 2010, Yeh et al., 2014). Improved geophysical tools to help quantify such changes are always welcomed. An example of the usefulness of repeat airborne thermal infrared (TIR) surveys to monitor changes in steaming ground was recently demonstrated at the nearby Ohaaki Geothermal Field (Reeves et al., 2015). This paper describes research work in progress to improve the quantification of such heat-loss assessments using satellite thermal infrared data (TIRS), in combination with airborne TIR surveys and ground-based temperature and calorimetry measurements.

The Karapiti thermal area (also known as 'Craters of the Moon') is located within the Wairakei Geothermal Field, and is arguably one of the better studied areas of steaming ground in the world (Mongillo & Allis, 1988, Bromley & Hochstein, 2001, 2005, Hochstein & Bromley, 2001, 2005, 2007, Mia et al., 2012). Heat is discharged directly by numerous fumaroles and steam vents, craters, and hot mud pools. Heat is also discharged in a diffuse convective manner and by conductive transfer through hot and warm ground, over an area of ~0.35 km^2 (Figure 1). The Karapiti thermal area contains extensive areas of hydrothermal clay deposits ('bare ground') and thermally-tolerant 'prostrate kanuka' scrub (light green in Figure 1). It is surrounded by radiata pine forests (dark green in Figure 1), which are occasionally logged (eastern side of Figure 1), exposing pumice-derived soil.

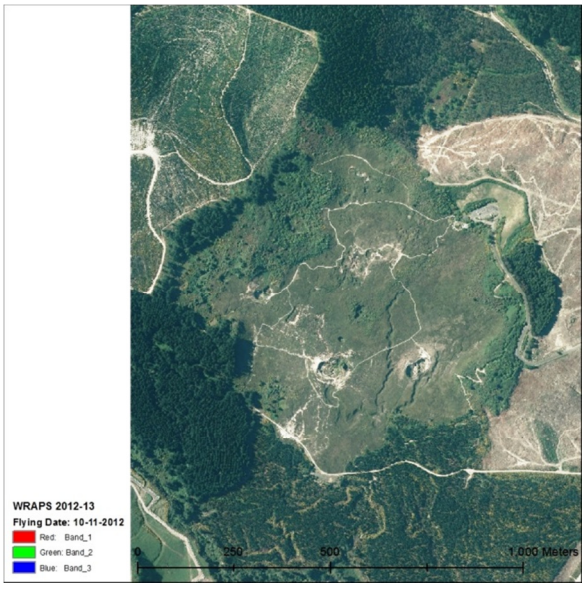

Figure 1: Satellite photo of Karapiti thermal area, (Waikato Region Aerial Photograph Syndicate, 10 Nov 2012); area matches figures 2-7.

This paper provides for comparison new estimates of heat loss from the Karapiti thermal area using satellite imagery (section 2), aerial thermal infrared imagery (section 3) and ground-based temperatures with calorimetry (section 4).

2. SATELLITE THERMAL INFRA-RED

Landsat-8's Thermal Infra-Red Sensor (TIRS) data (http://landsat.usgs.gov/landsat8.php) has recently become available for monitoring and thermal characterization purposes (replacing its predecessors Landsat-7 and Landsat-5). Such data can potentially be used to calculate Radiative Heat Flux (RHF) from areas of geothermally-heated ground. Analysis involves simultaneous processing of multispectral (OLI – Optical Land Imager) and thermal (TIRS) data. The procedure is summarized in the following eight steps (2.1 to 2.8), using satellite imagery from Karapiti. The imagery (at 30m x 30m pixel size) was obtained on 17 Jan. 2014 at 22:01 UTC (11:01 local time).

2.1 Digital Number to Surface Reflectance

Landsat-8 data is freely available from the USGS in 16-bit unsigned integer format. The images (or 'scenes') use UTM coordinates (zones 1-60N) and the Southern hemisphere data are represented with negative northings. Its "Surface Reflectance" data is acquired from the USGS EarthExplorer (EE) website. The Landsat 8 Surface Reflectance product is computed using specialized software called L8SR. It is provisional software and its results have not been completely validated; however, this method is potentially more robust in removing local atmospheric effects due to the presence of clouds, cloud shadows, and snow in the data (Zhu and Woodcock, 2012). This provisional method currently uses the solar zenith and view zenith angles at the scene centre for calculations as part of the atmospheric correction.

Figure 2 illustrates spectral radiance data using an image of the Karapiti area, which shows multispectral channels of near infrared (NIR), Green and Blue, displayed as red–green-blue respectively, for surface reflectance (SR) data.

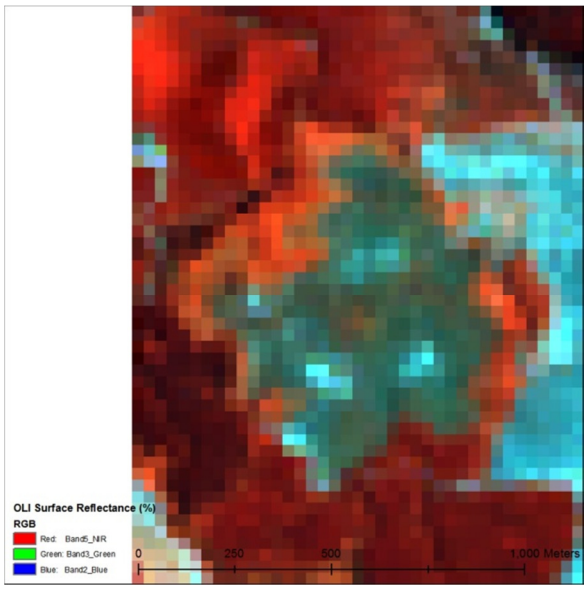

Figure 2: Three bands (NIR, Green, Blue) of corrected SR values at Karapiti (30m x 30m pixels)

2.2 Computation of Vegetation Index

Vegetation health is related to biomass, chlorophyll concentration and water stress, and can be assessed in satellite imagery through computing the Normalized Difference Vegetation Index (NDVI) (Mia et al., 2012):

$$NDVI = (SR_1-SR_2)/(SR_1+SR_2)$$

where SR_1 & SR_2 are surface reflectance of near-infrared and red bands respectively.

The NDVI values range from -1 to +1. Green vegetation has high values, water has negative values and bare ground has a value around zero. As a normalized index, NDVI is not affected by any changes in illumination conditions, surface or aspect. The NDVI image of the Karapiti atmospheric-corrected SR data in Figure 3 illustrates the difference between bare ground (purple), thermally-stressed vegetation (light green to yellow) and mature forest (dark green).

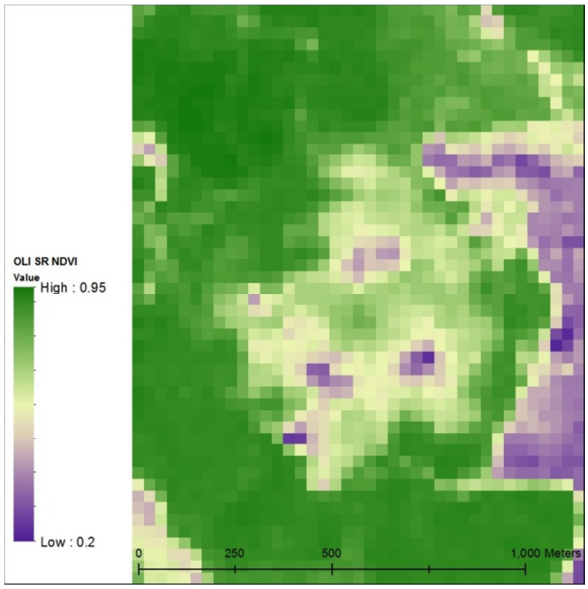

Figure 3: NDVI image at Karapiti (0.2 – 0.95)

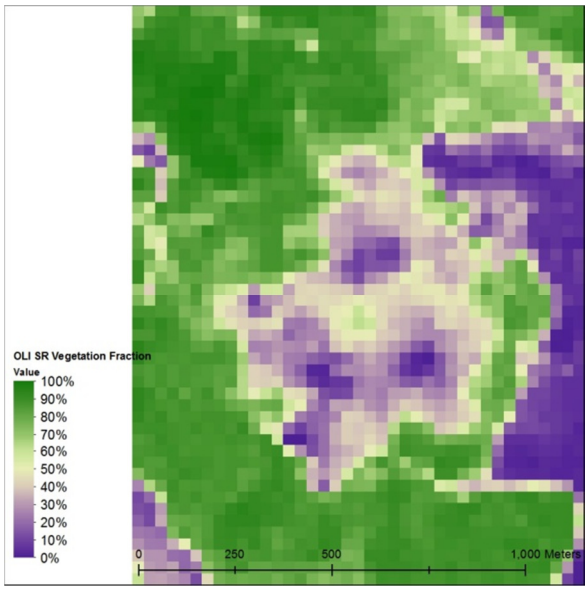

Figure 4: NDVI based fractional vegetation map. Purple pixels represent up to 40% bare ground

The central purple areas of Figure 3 coincide with steam-heated craters (Figure 1), whilst the area along the eastern edge of the image was recently logged. The NDVI is also used to estimate Fractional Vegetation (FV) which is the

percentage of vegetation distributed within a pixel (Brunsell and Glllies, 2002):

$$FV = [(N_{pixel}-N_{min})/(N_{max}-N_{min})]^2$$

Where N = NDVI; minimum or maximum values are scene-specific and refer to known areas of bare ground and thick vegetation, respectively. Figure 4 provides an example of a Fractional Vegetation map for Karapiti.

2.3 Computation of Emissivity

The fractional vegetation method was applied to estimate the surface emissivity of the image (Brunsell and Glllies 2002). Lower and upper limits for broad-band emissivity of bare ground and forest vegetation at Karapiti were chosen to be 0.96 and 0.98 (from Mia et al., 2012). The spatial distribution of emissivity at Karapiti is accordingly identical to that of Figure 4, but across a 0.96 to 0.98 range.

2.4 Conversion of Thermal Image into Temperature

Once the spectral radiance (surface reflectance, SR) and surface emissivity values for a scene have been determined, the next processing steps convert Thermal Infra-Red Sensor (TIRS) data into Land Surface Temperature (LST).

TIRS band data are converted into Top of Atmosphere (TOA) Spectral Radiance values using the radiance rescaling factors provided in the metadata file. These are then converted into TOA brightness temperatures in Kelvin (T_s) using (from Barsi et al., 2003):

$$T_s = K_2/(\ln(K_1/L_\lambda+1)$$

where, K_1 and K_2 are band-dependent thermal conversion constants from the metadata, and L_λ is spectral radiance for each band in W m^{-2} sr^{-1} μm^{-1}.

2.5 Computation of Land Surface Temperature

Land Surface Temperature (LST) is the key variable to be retrieved from the TIRS data (Jimenez-Munoz et al., 2009). The correction of atmospheric attenuation and surface emissivity effects from TIRS data is an essential step. Neglecting the atmospheric correction will result in systematic errors in the predicted surface temperature. With no atmospheric correction, the predicted temperatures are typically 5-10 ^oK too low (Barsi et al., 2003).

For the Karapiti example discussed here, various processing methods are applied to the data so they may then be compared (Table 1). For reference, Method 1 in this table uses the raw "Brightness Temperature" without correction for atmospheric attenuation or surface emissivity effects.

There are two parallel LST processing options for Landsat-8 thermal data in order to account for atmospheric absorption effects.

a) Mono-window algorithm: this method processes data from a single channel. Since the TIRS-1 (Band 10) is located in a relatively low atmospheric absorption region of the spectrum (high atmospheric transmissivity values), it is preferable to use this channel for the single channel processing (Jimenez-Munoz et al., 2014).

b) Split-window algorithm: this method uses both thermal bands (10 & 11) of Landsat-8 data to determine the LST. Atmospheric absorption attenuates incoming radiance to the sensor, and the split-window technique assumes that the attenuation is proportional to the radiance difference of simultaneous measurements at two different wavelengths (Jimenez-Munoz et al., 2014, McMillin, 1975). This method is therefore considered superior because it is independent of local atmospheric attenuation assumptions.

The application of LST retrieval using mono-window algorithm is discussed in 2.6, while the split-window algorithm is discussed in 2.7.

2.6 Mono-window Algorithm

NASA's Atmospheric Correction Parameter Calculator (http://atmcorr.gsfc.nasa.gov/) uses MODTRAN (MODrate resolution atmospheric TRANsmission) code to model atmospheric propagation of electromagnetic radiation and returns atmospheric transmittance, up-welling and down-welling radiances at a given location as needed.

In the Karapiti example, optional inputs to the calculator (such as surface pressure and relative humidity) are obtained using NIWA's CliFlo climatic database (http://cliflo.niwa.co.nz/) for the nearest climate station (Taupo AWS) while the surface temperature was obtained from GNS Science Wairakei office data. The surface condition values used in the calculator and its returned atmospheric parameters are listed in Table 1.

Table 1. User input surface conditions and returned atmospheric correction parameters.

Input Surface Conditions	
Surface altitude	0.385 km
Surface pressure	970.5 mb
Surface temperature	17.3 ^oC
Surface relative humidity	40.6 %
Atmospheric Correction Parameters	
Average atmospheric transmission	0.94
Bandpass upwelling radiance	0.47 W m^{-2} sr^{-1} μm^{-1}
Bandpass downwelling radiance	0.85 W m^{-2} sr^{-1} μm^{-1}

Three different methods for mono-window atmospheric correction incorporating land-surface emissivity variations have been considered. They include formulations published by Barsi et al. (2003) (Method 2), Qin et al. (2001) (Method 3) and Jiménez-Muñoz & Sobrino (2003) (Method 4).

Method 2 requires in-situ, radio-sounding data to be recorded simultaneously with the satellite passes in order to correct for local atmospheric transmittance parameters. Such data is not available at Karapiti. Method 3 was developed for Landsat-5 data to avoid the need for radio-soundings. It was used by Mia et al. (2012) to process Landsat-5 and Landsat-7 data in order to demonstrate the potential usefulness of satellite infrared data for long-term surface heat-flux monitoring. Variables required to calculate a corrected LST include land surface emissivity, total atmospheric transmittance, near-surface air temperature, and sensor brightness temperature.

Method 4 requires similar input data, and has been adapted by Jiménez-Muñoz et al. (2014) for use with Landsat-8 TIRS. LST results for Karapiti are illustrated in Figure 5.

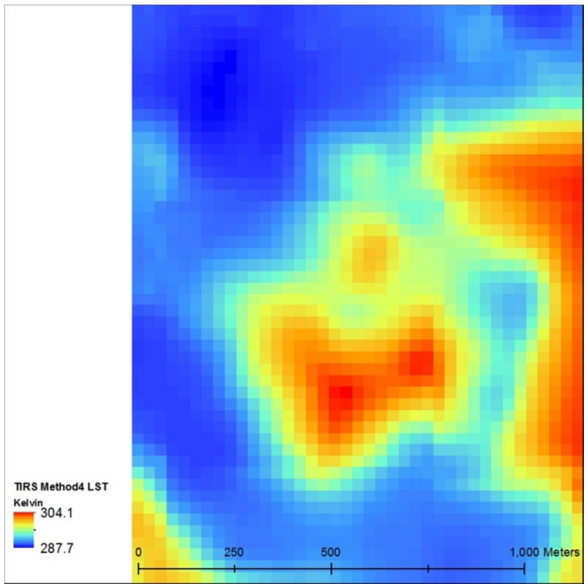

Figure 5: Land Surface Temperature (^{o}K) using mono-window algorithm, Method 4 (14.5 – 30.9 ^{o}C).

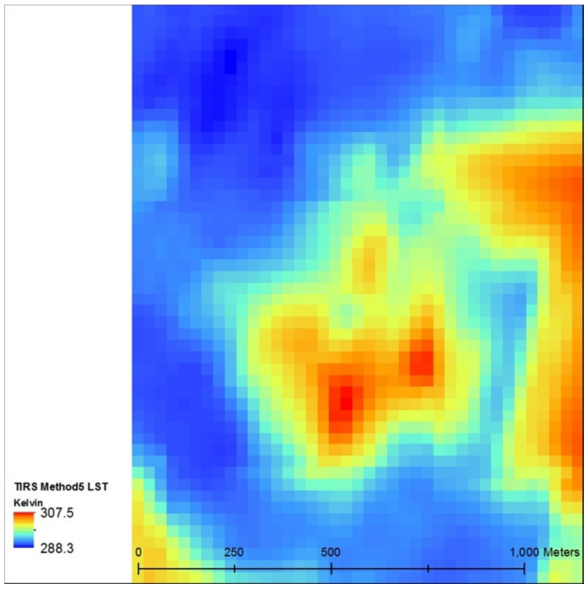

Figure 6: Land Surface Temperature (^{o}K) using split-window algorithm, Method 5 (15.2 - 34.4 ^{o}C)

2.7 Split-Window Algorithm (Method 5)

The LST (T_s) split-window algorithm, as applied on Landsat-8 TIRS data, and described in Sobrino & Raissouni (2000) is as follows:

$$T_s=T_i+c_0+c_1(T_i-T_j)+c_2(T_i-T_j)^2+(c_3+c_4w)(1-\varepsilon)+(c_5+c_6w)\Delta\varepsilon$$

where, c_0 to c_6 are coefficients, T_i & T_j are sensor brightness temperatures (^{o}K) at split window bands i & j, E is mean emissivity, $\Delta\varepsilon$ is emissivity difference (i-j), and w is total atmospheric water vapour content (g/cm^2). Values for c_0-c_6 were determined by Jimenez-Munoz et al. (2014) from simulated data, and for convenience are listed here in numerical order (c_0 to c_6):

-0.268, 1.378, 0.183, 54.3, -2.238, -129.2, 16.4.

For Karapiti, w is 5.6 g/cm^2 as estimated from the same day AQUA MODIS image processed to Level-2 Atmosphere Water Vapour data (Gao, 2015). That causes a rise in LST value of about 0.82 to 1.65 ^{o}K for different emissivity values. ε ranges between 0.96 and 0.98, but between different bands $\Delta\varepsilon = 0$. The results are plotted in Figure 6.

2.8 Calculation of Radiative Heat Flux

Theoretical Radiative Heat Flux (RHF), is calculated using the Stefan –Boltzmann equation,

$$Q_r = \tau\,\sigma\,\varepsilon\,A\,(T_s^4-T_a^4)$$

where; Q_r = RHF (W/m^2), τ = atmospheric transmissivity, σ = Stefan–Boltzmann constant, ε = emissivity, A = area (m^2), T_s = LST (^{o}K), and T_a = ambient temperature (^{o}K).

The spatial distributions of RHF at Karapiti using different processing methods have been compared; an example for the split window algorithm is presented in Figure 7.

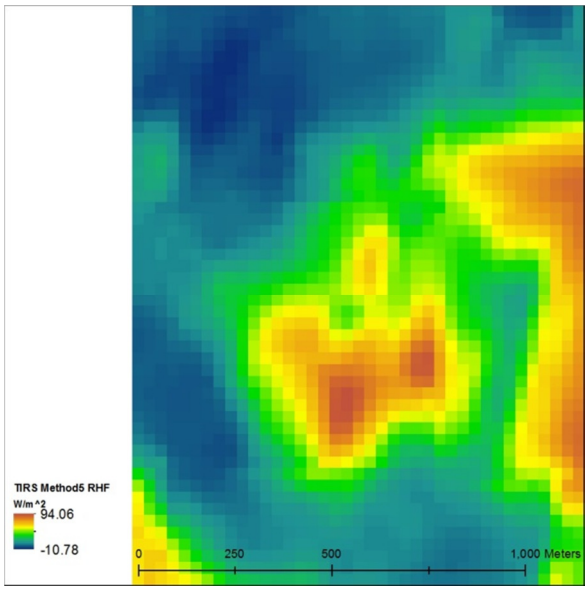

Figure 7: Radiative Heat Flux (W/m2) using split-window algorithm (calculated from Figure 6)

For the purposes of this comparison, Table 2 summarizes the results of the calculations using five different methods, as described above, for the Karapiti image. The minimum and maximum calculated pixel values for land surface temperature, and radiative heat flux, are listed along with the summed (positive) RHF values across the area of the scene, in MW.

Table 2. Comparison of LST calculation methods and RHF results (see text for method descriptions).

Process Method	LST Min.	LST Max.	RHF Min.	RHF Max.	RHF Total
	^{o}K	^{o}K	W/m^2	W/m^2	MW
1	286.5	300.7	-19.6	54.8	20.3
2	287.6	304.0	-14.1	72.9	32.8
3	288.1	304.6	-11.7	76.7	36.6
4	287.7	304.1	-14.1	73.3	33.1
5	288.3	307.5	-10.78	94.1	42.8

Note, the method does not differentiate between re-radiated solar heat and shallow heat of geothermal origin for the total radiated heat flux. For example, the strong anomaly

along the eastern border of Figure 7 is clearly not caused by any geothermal heat-flux but is instead a reflected and residual solar radiation heating effect (for a late-morning image) on the recently-logged bare ground. Ground-truthing of the source of apparent thermal anomalies is therefore still a necessary part of interpretation.

Method 1 (without any corrections) results in anomalously low temperatures and heat flux. Method 5 is preferred because it is least dependant on external factors. However, determination of the local atmospheric transmissivity (moisture content) at the time of data capture remains one of the largest sources of uncertainty in LST and RHF.

3. AIR-BORNE THERMAL INFRA-RED

Aerial thermal infrared (TIR) data in digital format were collected over Karapiti thermal area on the night of 26/2/2014 using a FLIR A615 TIR camera mounted to a fixed-wing aircraft. This was part of a larger survey of the Wairakei-Tauhara Geothermal Field conducted for Contact Energy Ltd. TIR images consist of 16-bit 'tif' image files. These were mosaicked and geo-registered to aerial photography resulting in a ground pixel size of c. 0.7m. The resulting composite image of Karapiti is shown in Figure 8.

Inferred surface temperatures are derived from the raw data by developing a calibration equation between the TIR data and water temperatures measured at 19 sites during the survey. It is acknowledged that different ground cover (pumice soil or vegetation) results in slightly different emissivities from that of water and this will result in small differences between inferred and actual surface temperatures.

Three methods modified from Bromley et al. (2011) are used to estimate heat flux from the TIR data. The first method (Method 2 in Bromley et al., 2011) uses an empirical relationship between TIR inferred surface temperatures and boiling point depths at each pixel derived from data collected at Karapiti and Tauhara monitoring sites (Hochstein & Bromley, 2005). An empirical method relating boiling point depth to heat flux is then used to estimate heat losses. Two sub-method variations are trialled here (2a and 2b):

a) The pixels in the study area are divided into 2 ^{o}C temperature bands with the midpoint of each band taken as representative. The total area for each band is calculated using the pixel area of 0.49 m^2, and the results summed. Only the heat flux for inferred ground temperatures ≥ 18 ^{o}C (i.e. ~6 ^{o}C above ambient) is reported because lower temperatures tend to be noisy and subject to effects such as vegetation screening and residual solar heating. Ambient ground/air temperatures are assumed to be 12.6 ^{o}C, which was the mean air temperature during the TIR survey.

b) The equations are applied directly to each pixel for all pixels ≥ 18 ^{o}C, without binning. Selected pixels that are clearly not due to geothermal influences are discarded.

The next method (Method 3 in Bromley et al., 2011), uses a direct empirical relationship between inferred TIR temperature and heat flux:

$$Q = 50.3*(T_{(inferred)} - T_{(ambient)}) - 148 \text{ W/m}^2$$

This is multiplied by pixel area and summed to determine total heat flux. As for the previous method, two variations are used; one with the TIR data split into 2 degree bins (a), and the other using all individual pixels (b).

The final method (Method 4 in Bromley et al. (2011) calculates the theoretical heat fluxes from anomalously hot ground (≥ 18 ^{o}C), directly from the inferred TIR ground temperatures. The radiative component uses the Stefan–Boltzmann equation, and the still-air convective heat transfer component uses a coefficient of 11 Wm^{-2}K^{-1}). This is calculated for each valid pixel and summed to give a total heat flux.

Although the Karapiti area is dominated by heated ground, with no water discharges, it is acknowledged that there are also many fumaroles and diffuse steam discharges, whose convective flux is not accounted for in these radiative and conductive heat flux calculations. Such discharges significantly increase the total heat flux. For example, Bromley & Hochstein (2005) assessed the convective heat losses in 2004 to be about 107 MW from fumaroles and 69 MW from diffuse steam discharges, leaving 69 MW (or 28% of the Karapiti total of 245 +/- 20 MW) originating from conductive and then radiative heat losses.

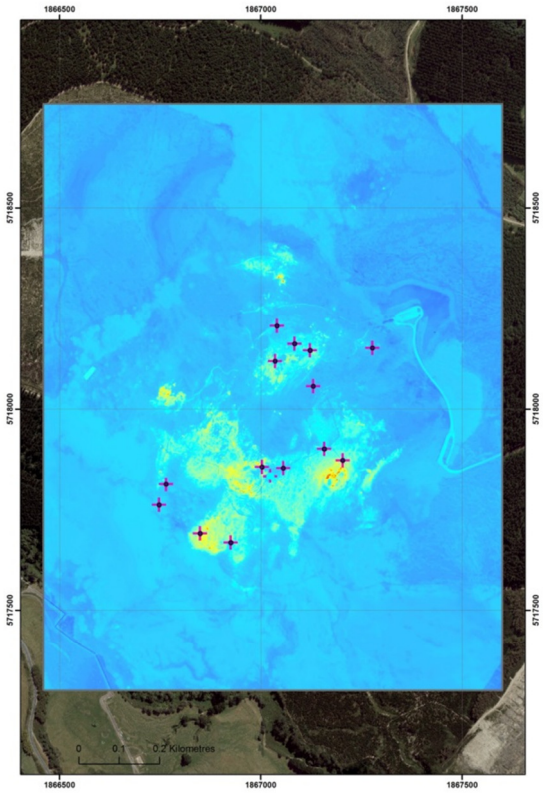

Figure 8: Air-borne thermal infrared image of Karapiti. Yellow to red areas are hotter. "+" labels are calorimeter sites (section 4). Eastern-side tar-seal road shows residual solar heating.

Table 3 summarises the conductive/radiative heat loss from the Karapiti thermal area using each method applied to the 2014 TIR data for surface temperatures ≥ 18 ^{o}C. The range in estimates is 20 to 51MW. Methods 2 and 3 use empirical relationships derived from similar datasets and so are expected to be similar in magnitude. Method 4 is based on theoretical radiation heat loss and still-air convection, so may not adequately account for ground surface cooling (and therefore heat-loss) caused by wind. Also, all of these

methods will be under-estimates because they neglect the heat losses arising from the large areas of warm ground between ambient and 18 °C (mostly beneath ~0.5-2m thick vegetation cover consisting of prostrate kanuka).

Table 3. Total conductive-radiative heat flux at Karapiti for ground temperatures ≥ 18°C using TIR.

Method:	2a	2b	3a	3b	4
Conductive heat-flux (MW)	51.4	51.0	48.5	48.1	20.6

4. GROUND-TEMPERATURE & CALORIMETRY

In conjunction with the air-borne TIR survey described in section 3, fifteen surface heat flux measurements were undertaken at Karapiti (Figure 9) during February 2014, using a water-calorimeter to determine total and convective surface heat flux. These measurements were accompanied by ground temperatures taken at depths of 0.05, 0.1, 0.15, 0.2, 0.25, 0.5 and 1.0 m, using a K-type thermistor, to determine temperature gradients and boiling point depths. Surface temperatures were taken using a hand-held infrared thermometer. Attempts to determine the amount of vapour emitted from the ground surface were undertaken using two techniques: (1) collection of condensed liquid on the base of the calorimeter using a dried and pre-weighed tissue; and (2) absorption of moisture by dried and pre-weighed desiccant. Neither method produced satisfactory results, as 'control' samples were found to gain moisture throughout the day, despite storage in a cooled dry container.

The calorimeter records linear increases in temperature of water, starting from near-ambient conditions, caused by steady ground heat transfer over, for example, a 5 minute period. This allows a total heat flux from the surface to be determined. Increase in water temperature while the calorimeter is slightly elevated (on a 2 cm ring) over a similar period of time (5 minutes) allows the non-conductive (radiation and convection) heat flux from the surface to be determined. Before, after, and in-between ground and elevated measurements, the calorimeter is left on a thick wooden block to measure the background influence of the surrounding atmosphere (at ambient temperature). Temperatures on the lid of the calorimeter are also continuously recorded to allow correction, if necessary, for ambient temperature changes. Figure 10 shows an example of the recorded temperature in the water-filled calorimeter over a total site occupation period of about 20 minutes.

The total heat flux from the ground is determined from the temperature gradient with time ($\frac{\Delta T_g}{\Delta t}$) measured while the equipment is placed directly on the surface, and multiplying it by the mass of the water within the calorimeter (m), and the specific heat capacity of water (c), divided by the total area (A) of ground covered by the calorimeter.

$$q_{tot} = \frac{mc\left(\frac{\Delta T_g}{\Delta t} - \frac{\Delta T_{lid}}{\Delta t}\right)}{A}$$

where $\frac{\Delta T_{lid}}{\Delta t}$, is the change in temperature recorded by the lid sensor over time, and is used as a proxy for any heating / cooling influence from the ambient air temperature.

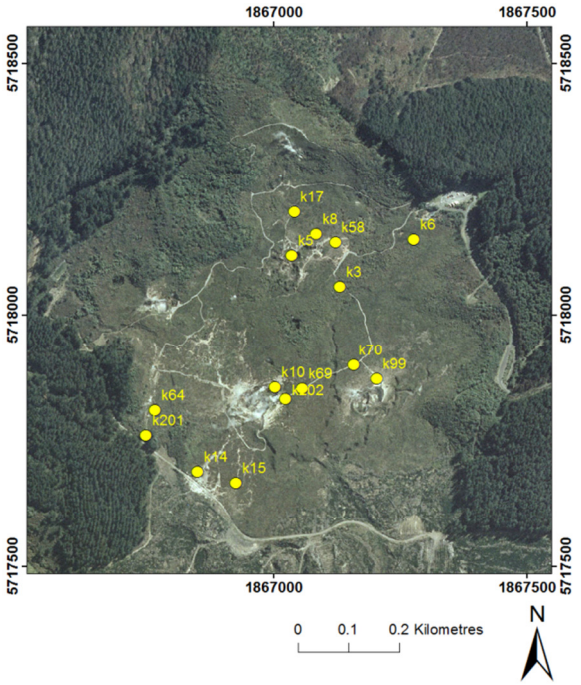

Figure 9: Location of ground surface heat flux measurements at Karapiti in 2014.

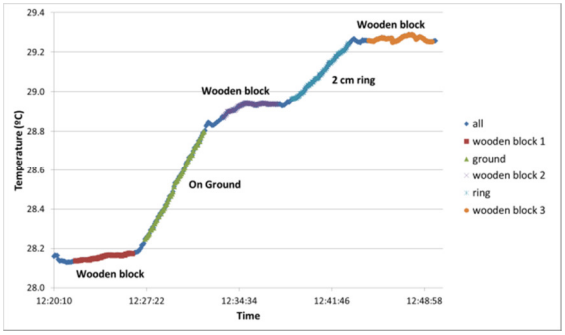

Figure 10. Calorimeter temperature log at site k70.

Convective heat flux is estimated by collecting the moisture gathered on the base of the calorimeter (or in a container of desiccant) while it is elevated on the 2 cm ring. (There is a large error associated with these estimates because of incomplete moisture capture and subsequent evaporation).

$$q_{conv} = \frac{\frac{\Delta mc}{\Delta t}}{A}\left(h_g - h_c\right) + L$$

Where $\frac{\Delta mc}{\Delta t}$ is the change in mass of the tissue, $h_g$is the specific enthalpy of steam, h_c is the enthalpy of the droplets, and L is the liquid loss component.

Conductive heat flux is determined by multiplying the temperature-depth gradient by the thermal conductivity.

$$q_{cond} = \frac{\Delta T}{\Delta z}\kappa(z)$$

An average thermal conductivity (κ) of the soil at Karapiti of 0.7 W/mK is assumed. This value can be improved by collecting shallow soil samples and undertaking thermal properties testing (Seward & Prieto, 2015, Van Manen &

Wallin, 2012). Based on previous studies, the key variable is soil moisture (Bromley & Hochstein, 2001).

Radiative heat can also be determined by

$$q_{rad} = \varepsilon_g \sigma(T_g^4) - \alpha_p \sigma(T_w^4)$$

Where ε_g is the emissivity of the ground, α_p is the absorptance of the calorimeter base-plate, σ is the Stefan-Boltzman constant and *Tw* and *Tg* are the temperature of the water within the calorimeter and the ground temperature, respectively. This is the heat transfer component that is detected by the remote sensing methods. Further work into determining the emissivity of the ground of both bare soils and ground covered with vegetation needs to be undertaken to be able to relate ground observations to remote measurements.

The depth to boiling point at each site is also calculated by:

$$z = \exp[c_1(T_{BP} - T_z)]$$

where c_1 is an empirically derived constant (-0.025 at Karapiti, Hochstein & Bromley, 2005).

Figure 11 shows how the boiling point depths at repeated sites have changed over time (updating Mia et al., 2012) Table 4 lists the processed Karapiti heat-fluxes and boiling-point depths collected in February 2014.

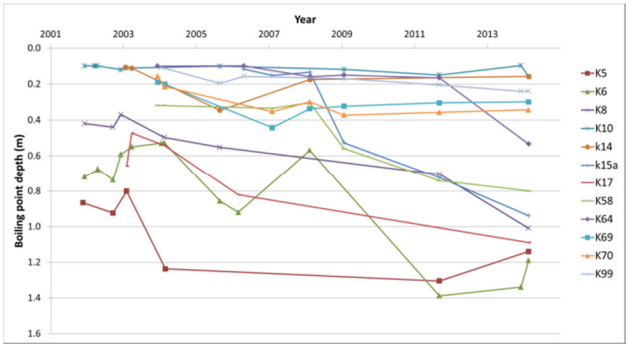

Figure 11: Changes in Boiling Point Depth since 2001

Table 4 : Calorimeter Heat-flux Data (17-19/2/14)

	Ground heat-flux W/m^2			Ring (2 cm) flux W/m^2			
site	**Tot-al**	**Cond-uctive**	**Radia-ted**	**Tot-al**	**Conv-ective**	**Radi-ated**	**Z-bp**
K64	270	236	50	126	5.5	38	0.53
K15	613	318	63	204	13	55	0.94
K10	404	472	74	145	0	66	0.16
K58	139	198	11	33	0	12	0.8
K69	158	305	47	94	1.8	41	0.3
K70	187	270	23	96	-1.8	22	0.34
K99	310	295	31	203	-1.8	36	0.24
K3	-18	-13	1.0	-13	-1.8	-1	10
K5	143	149	38	85	3.6	34	1.14
K6	54	151	9.5	51	0	10	1.19
K8	175	181	35	112	0	34	1.01
K14	403	398	82	138	5.5	69	0.16
K17	135	142	50	72	1.8	37	1.09
K201	-21	-5.3	-2.8	-28	0	-3.4	10
K202	61	134	23	25	-1.8	17	1.2

5. CONCLUSIONS

Improved processing methods are being investigated to enable better use of remote sensing techniques for monitoring changes in surface geothermal features, especially large areas of steam-heated ground. Satellite data, along with high-resolution air-borne infrared surveys and repeat ground measurements of shallow temperatures and calorimeter heat-fluxes, are expected to achieve a long-term improvement in the quantification of natural and induced changes in surface heat loss. This will assist in calibrating reservoir simulation models that are becoming ever more sophisticated at matching and predicting the effects on surface thermal features of different reservoir development scenarios.

Satellite infrared data processing issues are currently being addressed. These include: accounting for surface emissivity variations; calibration using known surface temperatures; correction for ambient (background), reflected and residual solar radiation effects; and optimizing atmospheric correction algorithms (split or mono window). For combined interpretation of satellite TIRS, airborne TIR and ground-based heat-flux assessments, issues include accounting for convective heat-losses and spatial resolution problems.

Heat-loss assessments were made using both satellite and air-borne TIR data from the Karapiti thermal area at Wairakei. Issues to be further investigated here include better understanding of the reasons for differences in total heat-flux using different calculation methods (as listed in Tables 2 and 3).

Repeat calorimeter and ground temperature gradient measurements were made (Table 4) and compared with previous measurements at Karapiti (Figure 11). Improvements are sought to better quantify the convective component of heat loss (diffuse vapour discharge) and to further reduce uncertainties.

ACKNOWLEDGEMENTS

The authors are grateful for the support of Contact Energy Ltd in allowing the use of airborne infrared survey data for this study. Trustees and volunteers of the Craters of the Moon Charitable Trust are also thanked for facilitating access to undertake ground-based measurements over the past 14 years. This work forms part of GNS Science's Geothermal Research programme (GRN) funded by the Government of New Zealand.

REFERENCES

Barsi, J. A., Barker, J. L., Schott, J. R.: An Atmospheric Correction Parameter Calculator for a Single Thermal Band Earth-Sensing Instrument. *IGARSS03*, Centre de Congres Pierre Baudis, Toulouse, France, (2003).

Bromley, C.J. and Hochstein, M.P.: Thermal properties of steaming ground (Wairakei Field, NZ). Proc. 23rd New Zealand Geothermal Workshop, Auckland, New Zealand, pp.69-74, (2001).

Bromley, C.J. and Hochstein, M.P.: Heat discharge of steaming ground at Karapiti (Wairakei), New Zealand. *Proc. of the World Geothermal Congress 2005*, Antalya, Turkey, (2005).

Bromley, C.J., van Manen, S.M., Mannington, W.: Heat flux from steaming ground : reducing uncertainties. Proc. 36th Stanford Workshop on Geothermal Reservoir Engineering, Stanford University, California, pp. 925-931, (2011).

Brunsell, N. A., and Gillies, R. R.: Incorporating Surface Emissivity into a Thermal Atmospheric Correction. Photogrammetric Engineering & Remote Sensing, 68(12), pp.1263-1269, (2002).

Gao, B.C.: MODIS Atmosphere L2 Water Vapor Product. NASA MODIS Adaptive Processing System, Goddard Space Flight Center, USA*: http://dx.doi.org/10.5067/MODIS/MYD05_L2.006 (Aqua),* (2015)

Hochstein, M.P. and Bromley, C.J.: Steam cloud characteristics and heat output of fumaroles. *Geothermics*, 30(5): pp.547-559, (2001).

Hochstein, M.P. and Bromley, C.J.: Measurement of heat flux from steaming ground. *Geothermics*, 34(2): pp.133-160, (2005).

Hochstein, M.P. and Bromley, C.J.: Measurement of radiation losses over thermal ground using a calorimeter, Proc. 29th New Zealand Geothermal Workshop, (2007).

Jiménez-Muñoz, J. C., Cristobal, J., Sobrino, J. A., Soria, G., Ninyerola, M., Pons, X.: Revision of the Single-Channel Algorithm for Land Surface Temperature Retrieval from Landsat Thermal-Infrared Data. *Geoscience and Remote Sensing, IEEE Transactions*, 47(1), pp.339-349, (2009).

Jiménez-Muñoz, J. C. and Sobrino, J.: A generalized single-channel method for retrieving land surface temperature from remote sensing data. *Journal of Geophysical Research:Atmospheres*,108,D22 (2003).

Jiménez-Muñoz, J. C., Sobrino, J. A., Skokovic, D., Mattar, C., Cristobal, J.: Land Surface Temperature Retrieval Methods from Landsat-8 Thermal Infrared Sensor Data. *Geoscience and Remote Sensing Letters, IEEE*, 11(10), pp.1840-1843, (2014).

McMillin, L. M.: Estimation of sea surface temperatures from two infrared window measurements with different absorption. *Journal of Geophysical Research*, 80(36), pp.5113-5117, (1975).

Mia, M.B., Bromley, C.J., Fujimitsu, Y.: Monitoring heat flux using Landsat TM/ETM + thermal infrared data : a case study at Karapiti ('Craters of the Moon') thermal area, New Zealand. *Journal of Volcanology and Geothermal Research*, 235/236: pp.1-10, (2012).

Mongillo, M.A. and Allis, R.G.: Continuing changes in surface activity at Craters of the Moon thermal area, Wairakei. Proc. 10th New Zealand Geothermal Workshop, pp.345-349, (1988).

Newson, J.A. and O'Sullivan M.J.O.: Computer modelling of heat and mass flow in steaming ground at Karapiti thermal area, New Zealand. Proc. 29th Workshop on Geothermal Reservoir Engineering, Stanford University, California, (2004).

Newson, J.A.: Models of geothermal surface features at Wairakei. PhD Thesis, Engineering Science, Univ. of Auckland,http://researchspace.auckland.ac.nz, (2010).

Qin, Z., Karnieli, A., Berliner, P.: A mono-window algorithm for retrieving land surface temperature from Landsat TM data and its application to the Israel-Egypt border region. *International Journal of Remote Sensing*, 22(18), pp.3719-3746, (2001)

Reeves, R.R., Bromley, C.J., Milloy, S.F.: Using time series aerial thermal infrared surveys to determine near-surface thermal processes at the Ohaaki Geothermal Field, New Zealand. Paper 02009, *Proc. World Geothermal Congress 2015, Melbourne,* (2015).

Seward, A.M. and Prieto, A.M.: New Zealand rock properties : determining thermal properties of shallow soils. Paper 29013, *Proc. World Geothermal Congress 2015*, Melbourne, (2015).

Sobrino, J. A. and Raissouni, N.: Toward remote sensing methods for land cover dynamic monitoring: Application to Morocco. *International Journal of Remote Sensing*, 21(2), pp353-366, (2000).

Van Manen, S.M. and Wallin, E.: Ground temperature profiles and thermal rock properties at Wairakei, New Zealand. Renewable Energy. 34, pp.313-321, (2012).

Yeh, A., O'Sullivan, M.J., Newson J.A., Mannington W.I.: An Update on Numerical Modelling of the Wairakei-Tauhara Geothermal System. *Proc. 36th New Zealand Geothermal Workshop*, (2014).

Zhu, Z. and Woodcock, C. E.: Object-based cloud and cloud shadow detection in Landsat imagery. *Remote Sensing of Environment,* 118(1), pp.83-94, (2012).